AIAA 94-0403

Scalar Imaging Velocimetry Studies of the Dissipative Scales of Motion in Turbulent Flows

Lester K. Su and Werner J.A. Dahm

Department of Aerospace Engineering
The University of Michigan
Ann Arbor, MI

32nd Aerospace Sciences Meeting & Exhibit
January 10-13, 1994 / Reno, NV

Scalar Imaging Velocimetry Studies of the Dissipative Scales of Motion in Turbulent Flows

Lester K. Su[†] and Werner J.A. Dahm[††]

Gas Dynamics Laboratories, Department of Aerospace Engineering
The University of Michigan, Ann Arbor, MI 48109-2118

The concept of flow field velocimetry based on conserved scalar imaging measurements[1] is here applied to turbulent flow scalar field data to yield the first fully resolved, non-intrusive, experimental measurements of the spatio-temporal structure and dynamics of the full nine-component velocity gradient tensor field $\nabla\mathbf{u}(\mathbf{x},t)$ in a turbulent flow. We describe a variational method for implementing this concept, in which weighted residuals of the conserved scalar transport equation, the continuity condition, and a derivative smoothness condition are minimized over the space of velocity fields. The technique is applied to direct numerical simulation (DNS) data for the limiting case of turbulent mixing of a $Sc = 1$ passive scalar field. The spatial velocity fields $\mathbf{u}(\mathbf{x},t)$ obtained correlate well with the exact DNS results, as do statistics of the velocity and velocity gradient fields. The method is then applied to fully resolved four-dimensional $Sc \gg 1$ scalar field imaging measurements from a laboratory turbulent flow. Results give the time-varying (u, v, w) vector velocity component fields simultaneously everywhere on a regular three-dimensional spatial grid. Direct differentiation of these fields yields the spatial structure in the full velocity gradient tensor field components. From these, the vector vorticity field $\omega_i(\mathbf{x},t)$ and tensor strain rate field $\varepsilon_{ij}(\mathbf{x},t)$ are determined, as are the kinetic energy density field $k(\mathbf{x},t)$ and the kinetic energy dissipation rate field $\Phi(\mathbf{x},t)$. Finally, we demonstrate extraction of the time evolution of these fields by applying this scalar imaging velocimetry method to scalar field information at several sequential time steps.

1. Introduction

Information on the fully resolved, three-dimensional, spatial structure and simultaneous temporal dynamics of the full nine-component velocity gradient tensor field $\nabla\mathbf{u}(\mathbf{x},t)$ at the small scales of turbulent flows is key to the development of physical models for these scales of turbulence. These scales are generally presumed to be quasi-universal in high Reynolds number flows, and thus studied in a generic context. To date, this has been done almost exclusively via direct numerical simulations (DNS) of the Navier-Stokes equations. By comparison, experiments capable of directly yielding useful information on the detailed structure and dynamics of these scales have been few. Most have been limited to single-point measurements of a small subset of the full velocity gradient tensor field.

Non-invasive optical techniques have been increasingly used in recent years to measure certain velocity gradient components. Lang[2] (1985) developed an LDV with four focal volumes to measure the spanwise vorticity in a turbulent shear layer. More recent advances in laser diagnostics and high-speed data acquisition and processing capabilities have facilitated a variety of optically-based, non-intrusive velocimetry techniques which provide information over spatial fields of many points. Reviews of some of these are given, for example, by Adrian[3-4] (1986, 1991), Lauterborn & Vogel[5] (1984), and Gad-el-Hak[6] (1989). Being optically based, these techniques potentially offer high spatial and temporal resolution, as well as genuine field information rather than single-point. The most widely used are particle image velocimetry techniques. These generally produce two-

[†] Graduate Research Assistant, Student Member AIAA
[††] Associate Professor, Member AIAA

component velocity vectors over two-dimensional fields, though three-dimensional particle tracking[7-8] and holographic particle image velocimetry[9-11] are being developed for measuring full, three-component vector velocity fields in complex flows. However, as with all particle imaging techniques, the seeding densities required to adequately resolve the finest velocity gradient length scales in turbulent flows makes optical penetration into the flow difficult, and potentially limits these methods for studies of the fine structure and dynamics of velocity gradient fields in turbulent flows. This optical penetration difficulty can be circumvented by using an effectively continuous distribution of laser fluorescent dye molecules as the seed, whose size eliminates the Mie scattering associated with particulates and thus maintains optical transparency in the flow field. Determining velocities then no longer centers on finding discrete particle displacements, but rather on inversion of the time-evolving dye concentration field to extract the underlying velocity field. Often the dye molecules are both dynamically passive and conserved, so that the conserved scalar transport equation governs their concentration field evolution and extraction of the velocity field can begin from this equation. Such scalar based velocimetry techniques were first introduced in Ref. 1.

Here we demonstrate the first application of the scalar imaging velocimetry concept to laboratory measurements of a conserved scalar field in a turbulent flow, and extract the underlying velocity gradient tensor field as well as its time evolution. As before, we approach the problem of determining the fully resolved, space- and time-varying velocity field $\mathbf{u}(\mathbf{x},t)$ from the standpoint of the exact conserved scalar transport equation. A variational method for implementing this concept is described in Sec. II, in which weighted residuals of the conserved scalar transport equation, the continuity condition, and a derivative smoothness condition are minimized over the space of velocity fields. The technique is then applied in Sec. III to direct numerical simulation data for the limiting case of turbulent mixing of a $Sc = 1$ passive scalar field. The spatial velocity fields $\mathbf{u}(\mathbf{x},t)$ obtained are compared with the exact DNS results to assess the validity of the method. In Sec. IV, the method is then applied to fully resolved four-dimensional $Sc \gg 1$ scalar field imaging measurements from a laboratory turbulent flow. We extract the time-varying full vector velocity component fields simultaneously everywhere on a regular three-dimensional spatial grid. Direct differentiation of these fields yields the spatial structure in the full velocity gradient tensor field components $\nabla\mathbf{u}(\mathbf{x},t)$.

2. Variational scalar imaging velocimetry

In this section, we describe the scalar imaging velocimetry method used to determine the vector velocity field $\mathbf{u}(\mathbf{x},t)$ from fully resolved, four-dimensional measurements of a single, dynamically passive, conserved scalar field $\zeta(\mathbf{x},t)$ in turbulent flows. This implementation expands on that of Ref. 1 in its use of variational techniques in the velocity field extraction. The underlying conserved scalar field measurement technique will be reviewed here only briefly; details can be found in Refs. 12-15, 18.

A *Scalar field measurements*

Any dynamically passive conserved scalar field $\zeta(\mathbf{x},t)$ evolves via the advection-diffusion equation

$$\frac{\partial \zeta}{\partial t} + \mathbf{u}\cdot\nabla\zeta - \frac{1}{ReSc}\nabla^2\zeta = 0, \qquad (1)$$

where all quantities are normalized by reference length and velocity scales l^* and u^*. The dimensionless scalar diffusivity $1/ReSc$ (the inverse of the Peclet number) involves the Reynolds number $Re = (u^* l^*/\nu)$ and Schmidt number (ν/D), with ν and D being respectively the vorticity and scalar diffusivities. Scalar imaging velocimetry involves inversion of (1), together with additional conditions, based on measurements of the scalar field. The requisite measurements must therefore be fully resolved in both space and time, and have sufficient signal quality, to allow direct differentiation of the scalar field data to evaluate the derivatives appearing in (1).

Such fully resolved four-dimensional scalar field measurements are based on successive, high-speed, planar imaging of the laser induced fluorescence from a dynamically passive laser dye carried by the flow, whose concentration is a conserved scalar variable. A collimated laser beam is repeatedly swept through a small volume in the flow by a pair of low-inertia mirrors driven by two galvanometric scanners slaved to the imaging array timing. The successive 256 × 256 scalar field data planes are acquired at rates up to 142 planes/sec into gigabyte sized data sets using very fast computer disk ranks to produce a four-dimensional spatio-temporal data space. The resulting effective spatial resolution ($\Delta x, \Delta y, \Delta z$) between adjacent points in each three-dimensional data volume is smaller than the local strain-limited molecular diffusion scale $\lambda_D/\delta \sim Sc^{-1/2}Re_\delta^{-3/4}$ of the scalar field. Similarly,

the temporal resolution Δt between the same data point in successive spatial data volumes can be held smaller than the local molecular diffusion scale advection time λ_D/U. This resolution, together with the high signal quality attained, allows accurate differentiation of the measured conserved scalar field data in all three space dimensions and in time to determine the components of the instantaneous time derivative field $(\partial/\partial t)\zeta(\mathbf{x},t)$, the scalar gradient vector field $\nabla\zeta(\mathbf{x},t)$, and $\nabla^2\zeta(\mathbf{x},t)$ throughout the four-dimensional data space. Such fully resolved conserved scalar field measurements have been conducted at outer-scale Reynolds numbers $Re_\delta \equiv (U\delta/\nu)$ as high as 6,000. An example of a single three-dimensional spatial data volume obtained via this technique is shown in Fig. 1.

Note that, for dilute solutions in water, the scalar diffusivity of the dye is quite small, with $Sc \approx 2075$. As a consequence, the underlying velocity field which we are aiming to extract from such measurements is considerably smoother than the scalar field from which we begin. In particular, the finest gradient length scale λ_v in the velocity field is larger, by a factor of $Sc^{1/2}$, than the smallest gradient length scale λ_D in the scalar field. For the Sc in the laboratory data in Section IV, this ratio of scales is about 45. However, for the $Sc = 1$ DNS data in Section III, this ratio is only 1 and thus extraction of the velocity field is more difficult.

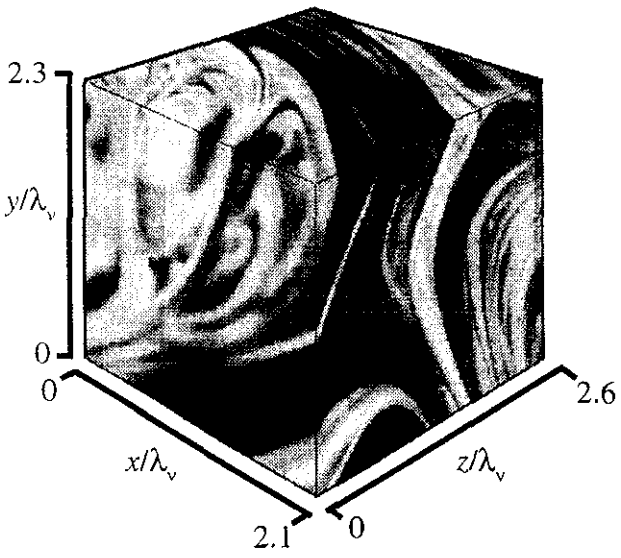

Figure 1. A sample three-dimensional data volume, from a turbulent jet with outer scale $Re_\delta = 3700$; from Southerland and Dahm[18].

B. *Formulation of the variational problem*

The relation between the scalar field and the underlying velocity field comes solely through $\mathbf{u}\cdot\nabla\zeta$ in (1) Previously[1, 15, 17], we have inverted this equation directly to obtain the local projection $u_{||}(\mathbf{x},t)$ of the velocity vector onto the scalar gradient unit vector, namely

$$u_{||}(\mathbf{x},t) \equiv \mathbf{u}(\mathbf{x},t)\cdot\frac{\nabla\zeta(\mathbf{x},t)}{|\nabla\zeta(\mathbf{x},t)|}. \qquad (2)$$

The full vector velocity field $\mathbf{u}(\mathbf{x},t)$ was then uniquely determined from the $\nabla u_{||}(\mathbf{x},t)$ field via an iterative scheme incorporating a smoothness assumption that becomes increasingly valid as Sc increases. The zeroth iteration estimate $\mathbf{u}^0(\mathbf{x},t)$ was found by direct inversion, at each point in the domain, of the local 3×3 linear system formed by writing (2) for triplets of closely spaced points having sufficiently noncolinear scalar gradients. Subsequent iterations incorporated the velocity gradients $\nabla\mathbf{u}^{n-1}(\mathbf{x},t)$ obtained from the previous iteration in the calculation of the n-th estimate $\mathbf{u}^n(\mathbf{x},t)$. Convergence was rapid, with the final result for $\mathbf{u}(\mathbf{x},t)$ typically achieved for $Sc \gg 1$ after just two or three iterations. This direct inversion implementation was shown to produce accurate results for a wide range of test cases – for details see Ref. 1.

Despite the high resolution and signal quality of the underlying scalar field measurements from Ref. 14, small but unavoidable errors will be introduced in the various scalar field derivatives in (1) and (2). As a consequence, even if the true $\mathbf{u}(\mathbf{x},t)$ were introduced in (1), the right hand side would not be exactly zero, as a direct result of these small errors in the $\zeta(\mathbf{x},t)$ derivative fields. Strict enforcement of the zero right side in (1) thus introduces errors in the velocity field obtained from this direct inversion approach. These considerations naturally motivate a variational approach to the inversion problem, in which the right side in (1) is not forced to zero, but is minimized over the space of possible velocity fields, subject to a smoothness constraint as before. That is, we take the velocity field $\mathbf{u}(\mathbf{x},t)$ that minimizes the integral of the right side of (1) over the entire domain as an optimal representation of the true velocity field. Formally, we minimize the integral of a function E over the domain D as

$$\int_D E(u_1,u_2,u_3;\,x_1,x_2,x_3)\,d^3\mathbf{x} = min, \qquad (3)$$

where E is composed of residuals representing deviations from conserved quantities, including (1), as well as

conditions measuring the smoothness in the $\mathbf{u}(\mathbf{x},t)$ solution.

C. *Specification of the variational equations*

As noted above, the integral minimization in (3) aims to find the one velocity field that best satisfies the scalar transport equation in (1) while at the same time satisfying an appropriate smoothness condition. In general, the function E can be written as a sum of an arbitrary number of such conditions

$$E \equiv E_1 + \alpha^2 E_2 + \beta^2 E_3 + \ldots, \tag{4}$$

where each of the $E_i \geq 0$ represents a local condition involving the velocity field and, possibly, the scalar field. The adjustable factors (α^2, β^2, ... > 0) allow control over the relative weights assigned to these individual conditions in the minimization function E. In our case, the term E_1 is chosen as the right side in (1), namely the condition that the (known) scalar field derivatives and any candidate velocity field be in "good" agreement with the scalar transport equation (1). Thus formally

$$E_1 \equiv \left\{ \left[\frac{\partial}{\partial t} + \mathbf{u}\cdot\nabla - \frac{1}{ReSc}\nabla^2 \right] \zeta(\mathbf{x},t) \right\}^2 . \tag{5}$$

The smoothness condition, as well as any additional conditions, must be specified in a manner consistent with the numerical scheme by which the minimum in (4) is to be found. In particular, writing (4) for a set of N discrete points in the domain D leads to a system of $3N$ simultaneous equations for the velocity components u_i for $i = \{1, 2, 3\}$ at each of the N points. In general this system will be very large. Consequently, we confine our interest to conditions that will produce a linear system, so that the simplicity afforded by linear inversion methods can be employed in the solution for $\mathbf{u}(\mathbf{x},t)$. This, in turn, demands that the derivatives $(\partial E_j/\partial u_i)$ should be linear in the components u_i, and thus that the conditions be at most second-order in $\mathbf{u}$. Among this restricted set of conditions, one is immediately obvious, namely the incompressibility condition $\nabla\cdot\mathbf{u} = 0$. This is represented in non-negative form as

$$E_2 \equiv \{\nabla\cdot\mathbf{u}\}^2 . \tag{6}$$

However while inclusion of this incompressibility condition is certainly desirable, it does not impart the requisite smoothness on the solution, and, together with (5), suffices to determine the solution in two dimensional flows only. An explicit smoothness condition is necessary. Ideally, this would be a direct mathematical representation of a specific physical property of the flow. Unfortunately, the existence of flow properties which can be represented as minimizations of integral quantities is very limited – e.g. to certain simple inviscid, circulation-preserving flows; see Truesdell[16]. Here we choose to minimize the velocity gradients by the condition

$$E_3 \equiv \nabla\mathbf{u}:\nabla\mathbf{u} . \tag{7}$$

The physical implications of this condition can be understood from the kinetic energy transport equation

$$\left[\frac{\partial}{\partial t} + \mathbf{u}\cdot\nabla - \frac{1}{Re}\nabla^2 \right] \frac{1}{2}\mathbf{u}^2(\mathbf{x},t) = -\mathbf{u}\cdot\nabla p - \frac{1}{Re}(\nabla\mathbf{u}:\nabla\mathbf{u}) . \tag{8}$$

The first term on the right is the work done by pressure forces, and the second term represents the net kinetic energy loss due to viscous stresses. Incorporating (7) as the smoothness condition thus drives the solution toward velocity fields for which the kinetic energy lost to viscous effects tends toward a minimum, as the fluid viscosity acts to smooth out strong gradients and pursues a condition of minimized kinetic energy loss.

Note that explicit agreement with these conditions is not being enforced; rather, we require only that the deviations from these conditions be minimized in the weighted sense prescribed in (3) and (4). Since the integral in (3) involves the three dependent variables u_i and three independent variables x_i, standard variational calculus leads to the three variational (Euler) equations

$$u\zeta_x^2 + v\zeta_x\zeta_y + w\zeta_x\zeta_z - \alpha^2\left(u_{xx} + v_{xy} + w_{xz}\right) - \beta^2\nabla^2 u = -\left(\frac{\partial\zeta}{\partial t} - \frac{1}{ReSc}\nabla^2\zeta\right)\zeta_x \tag{9}$$

$$u\zeta_x\zeta_y + v\zeta_y^2 + w\zeta_y\zeta_z - \alpha^2\left(u_{xy} + v_{yy} + w_{yz}\right) - \beta^2\nabla^2 v = -\left(\frac{\partial\zeta}{\partial t} - \frac{1}{ReSc}\nabla^2\zeta\right)\zeta_y \tag{10}$$

$$u\zeta_x\zeta_z + v\zeta_y\zeta_z + w\zeta_z^2 - \alpha^2\left(u_{xz} + v_{yz} + w_{zz}\right) - \beta^2\nabla^2 w = -\left(\frac{\partial\zeta}{\partial t} - \frac{1}{ReSc}\nabla^2\zeta\right)\zeta_z \tag{11}$$

where subscripts denote spatial derivatives. The solution of these equations gives the velocity field $\mathbf{u}(\mathbf{x},t)$ that minimizes (3) - (7) for the given scalar field data $\zeta(\mathbf{x},t)$. Note that these equations are linear in the velocity components (u, v, w).

Finding the solution for the velocity field involves discretizing (9) - (11) and writing these three equations for each of the points in each three-dimensional spatial data volume. In doing this we order the N points in each volume by indexing successively in x, y, and z. We then construct three N-dimensional vectors containing the velocity components u, v, and w at each of these points, and finally concatenate these to form a single $3N$-dimensional vector representing the velocity field $\mathbf{u}(\mathbf{x},t)$. The above equations can then be written as a linear system of the form $\mathbf{Au} = \mathbf{b}$, where $\mathbf{A}$ is a $3N \times 3N$ matrix containing the (known) scalar field derivatives appearing on the left in (9) - (11), and $\mathbf{b}$ is a $3N$-dimensional vector containing the scalar field derivatives on the right side in these equations. Solving for the unknown velocity field u simply requires inverting the matrix $\mathbf{A}$. However, owing to the size of this matrix in the cases presented here, direct solution methods are impractical. We therefore use standard linear iterative methods, in this case Gauss-Seidel and SOR iteration. The iteration is begun with $\mathbf{u} \equiv 0$ as the initial estimate.

Note that minimization of E_2 and E_3 in (6) and (7) can occur by reduction of the average velocity magnitude over the entire domain, as well as by reduction of the resulting scaled velocity gradients. The $\mathbf{u}$ in these conditions thus "floats." Inclusion of E_2 and E_3 in (4) will therefore reduce the average velocity magnitude by an amount that depends on α and β. It is only through E_1 that the average velocity magnitude tied to an absolute level set by the scalar field derivatives. The velocity field u that results from the above process is therefore finally reinserted in (3) to determine the uniform multiplicative constant that minimizes E_1 over the entire domain.

3. A DNS test for $Sc = 1$

In this section, the variational scalar imaging velocimetry method described above is applied to scalar field data obtained from a direct numerical simulation (DNS) of $Sc = 1$ passive scalar mixing in a turbulent flow. The velocity fields obtained through application of the scalar imaging velocimetry technique can be compared with the actual velocity fields used in the simulation, allowing us to quantify the accuracy of the technique.

We use the DNS data of Mell, Kosály & Riley[19] (1992) for turbulent mixing of a dynamically passive $Sc = 1$ conserved scalar quantity in a decaying, homogeneous, isotropic, incompressible, turbulent flow. The Taylor scale Reynolds number Re_λ decays from its initial value of 92 to 65 at the time chosen for this test. A sample scalar field plane from this simulation at this time is shown in Fig. 2. The computations were performed on a 128^3 volume. Scalar field derivatives were computed in $128 \times 128 \times 13$ point sub-volumes, which were then subsampled to $64 \times 64 \times 7$ point domains for this test. With $\Delta x = \Delta y = \Delta z$, the limited span in the third (z-) dimension was chosen to be characteristic of available fully resolved experimental scalar field data. The grid resolution was $\Delta x = 0.1\ \lambda_T$, and the time separation between successive volumes used in this test was $\Delta t = 0.07\ \lambda_T/|\mathbf{u}|_{rms}$, again to mimic the characteristics of currently available fully resolved experimental scalar field data.

The scalar field derivatives $\partial\zeta/\partial t$, ∇z, and $\nabla^2\zeta$ are the only inputs to the variational formulation in (9) - (11). These are obtained via linear central differences from the scalar field data. The velocity field is then obtained by inverting the linear system of (9) - (11) for the given scalar derivative matrix $\mathbf{A}$ and vector $\mathbf{b}$. For the volume dimensions used here, the vector $\mathbf{b}$ contains 86,016 elements. The Gauss-Seidel iteration on this system typically required about an hour on an HP9000/735 workstation. The resulting individual velocity vector component fields are shown in Fig. 3. Shown also in this figure are the actual DNS velocity vector component fields for comparison. It is evident by examining these that the variational scalar imaging velocimetry method yields

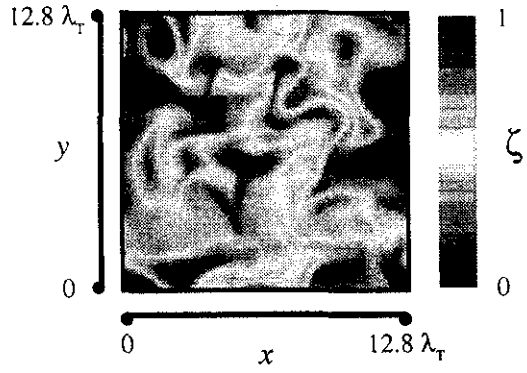

Figure 2. A sample scalar field plane from DNS of Sc = 1 scalar mixing in homogeneous, isotropic turbulence.

results for the velocity vector field which are in good agreement with the exact values. To quantify this agreement, we use the conventional fluctuation correlation

$$R_{AB} \equiv \frac{\overline{u'_A u'_B}}{\left(u'_A\right)_{rms}\left(u'_B\right)_{rms}} \qquad (12)$$

where the primes denote fluctuations, and the subscripts A and B refer to the SIV and DNS fields. The correlations obtained for the u, v, and w fields are 0.94, 0.94 and 0.91, respectively, where 1.00 represents perfect correlation. That the w component has the poorest correlation is not surprising, given that the data volume has only one-tenth the extent in the z-direction that it has in the x- and y-directions. Thus the one-sided velocity derivatives required at the limits of the volume are more likely to affect the accuracy of the z-direction velocity component than the others. Nevertheless, the correlation levels obtained are quite high. The departures from perfect correlation would appear to result primarily from the smoothness condition E_3 in (7), since the other two conditions in (3) should be identically zero.

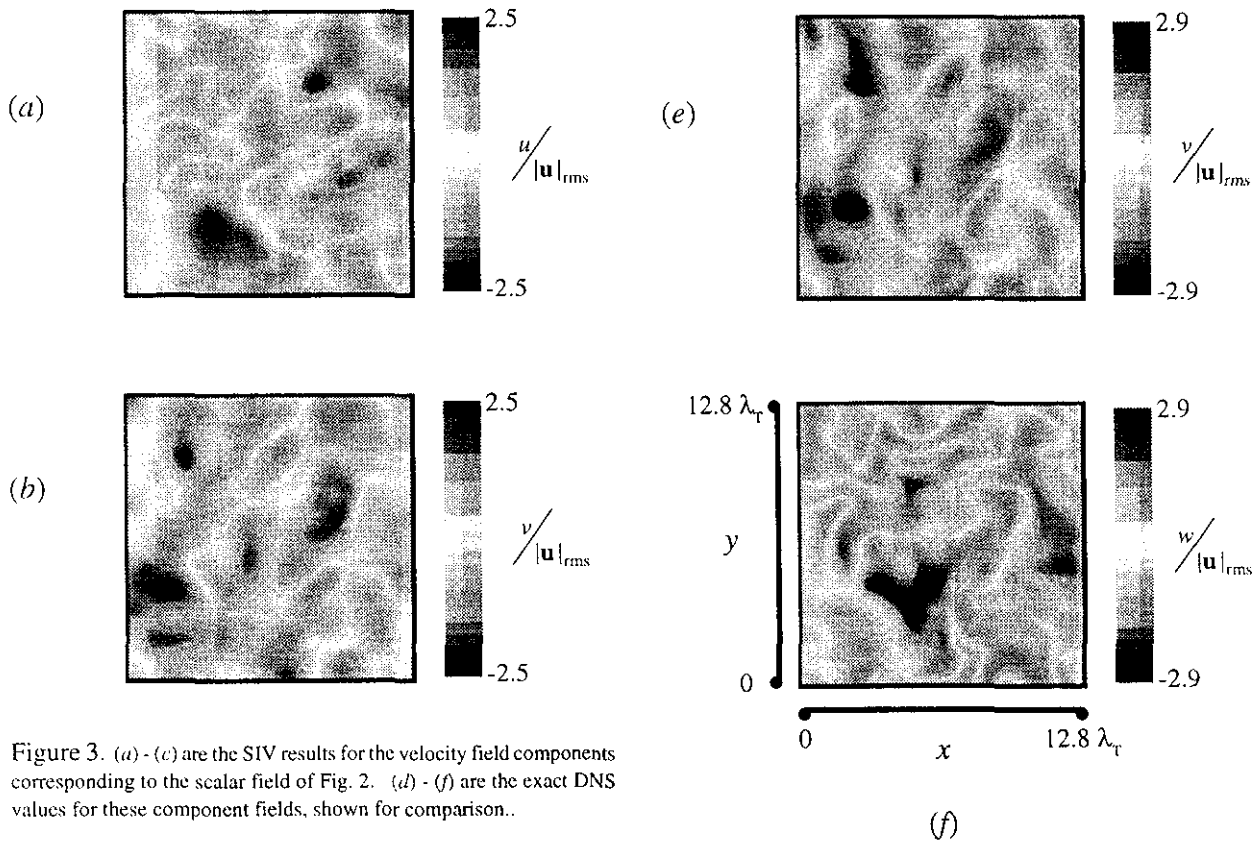

Figure 3. (*a*) - (*c*) are the SIV results for the velocity field components corresponding to the scalar field of Fig. 2. (*d*) - (*f*) are the exact DNS values for these component fields, shown for comparison..

As a further demonstration of the agreement between the DNS fields and the scalar imaging velocimetry results, Fig. 4 presents distributions of the values of the velocity components u, v and w for both the DNS and SIV fields. To emphasize that the important comparison is of the forms of the distributions, the velocity component values for each field have been normalized by their respective second moments. The similarity in the shapes of the distributions is evident.

It is salient to emphasize that this $Sc = 1$ test case is extremely demanding for any scalar-based velocimetry technique, since the scalar and velocity fields in this case have the same spatial length scales. The velocity field being sought therefore has the same degree of detail as does the scalar field, i.e. there is no redundancy of scalar field information. By comparison, at $Sc \gg 1$ the information content in the scalar field far exceeds that in the velocity field, and this redundancy should make extraction of the underlying velocity field even more accurate.

The primary interest in this scalar imaging velocimetry technique is the access it offers to the spatial structure and temporal dynamics of the full nine-component velocity gradient tensor. Accordingly Fig. 5 compares three typical components of $\nabla\mathbf{u}(\mathbf{x},t)$ with their DNS counterparts. Note that the structure and magnitudes of these tensor components is very similar in both cases. Indeed the visual comparison appears better than that in Fig. 3, however the quantitative correlations are actually lower. The complete tensor correlation $\Re_{AB}$ defined as

$$\Re_{AB} \equiv \frac{\overline{\left(\frac{\partial u_i}{\partial x_j}\right)_A \left(\frac{\partial u_i}{\partial x_j}\right)_B}}{\left\{\overline{\left(\frac{\partial u_i}{\partial x_j}\right)_A^2}\right\}^{1/2} \left\{\overline{\left(\frac{\partial u_i}{\partial x_j}\right)_B^2}\right\}^{1/2}} \qquad (13)$$

is 0.783. For the $\partial u/\partial y$, $\partial v/\partial z$, and $\partial w/\partial x$ component fields in Fig. 5 the correlations are 0.79, 0.83 and 0.75 respectively. The surprisingly better visual comparisons than in Fig. 3, for which the correlations are in fact significantly higher, apparently result from the larger number of features available as landmarks for comparison in the gradient fields.

Results such as those in Figs. 3 and 5 demonstrate

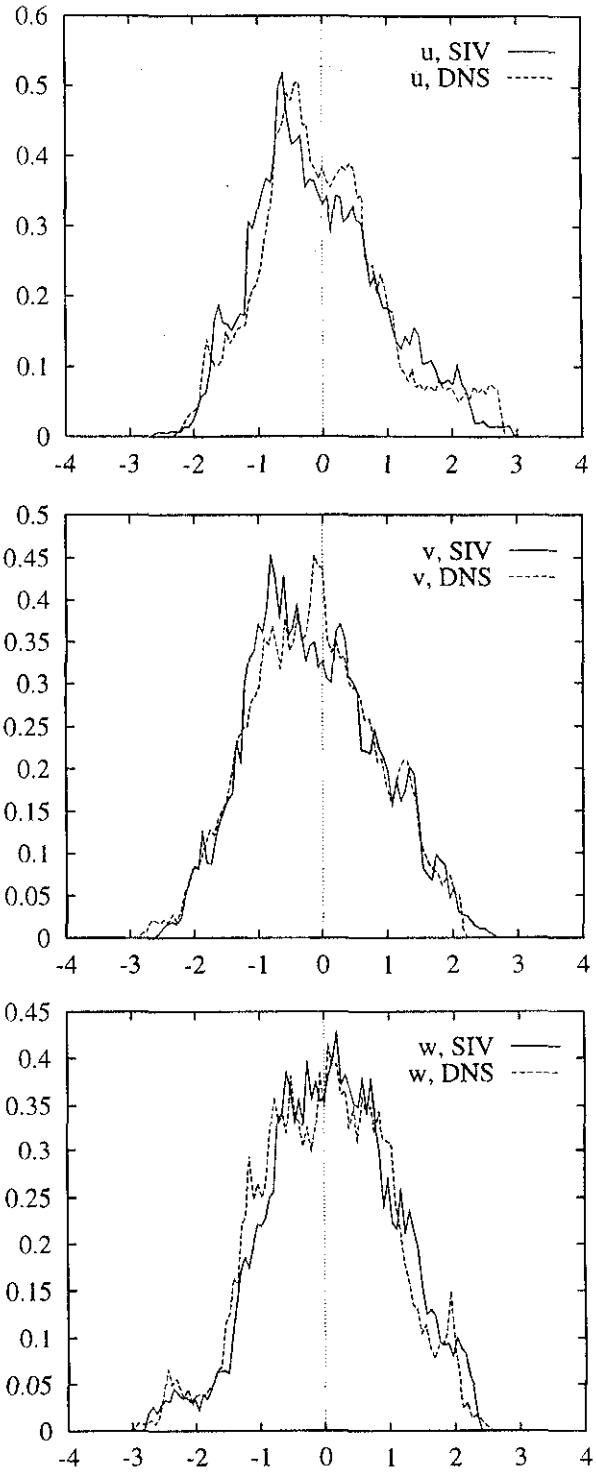

Figure 4. Pdf's of u/u_{rms} for the SIV results and the DNS fields. (top) the u-component pdf's, (center) the v-component pdf's, and (bottom) the w-component.pdf's.

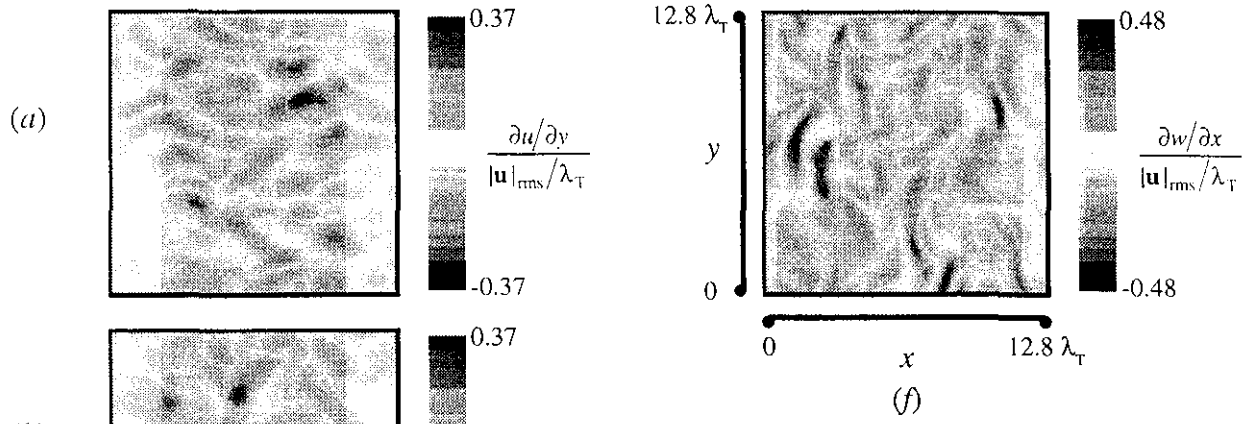

Figure 5. Components of the velocity gradient tensor for the SIV results of Fig. 3. (*a*) - (*c*) $\partial u/\partial y$, $\partial v/\partial z$ and $\partial w/\partial x$ for the SIV results. (*d*) - (*f*) the exact DNS fields, for comparison.

that, even in this limiting $Sc = 1$ case, the scalar imaging velocimetry method is capable of yielding rather accurate results for the spatial structure of the full vector velocity fields and nine-component velocity gradient tensor fields in turbulent flows. Since direct numerical simulations of turbulent mixing for $Sc \gg 1$ scalars are beyond present computational reach, similarly detailed DNS studies of the accuracy of scalar imaging velocimetry for large Sc scalar field data are not possible. We can, however, anticipate that extraction of the underlying velocity field is fundamentally more accurate for $Sc \gg 1$ than at $Sc = 1$, owing to the excess scalar field information available in the $Sc = 1$ case. Indeed, Ref. 1 demonstrated highly accurate extraction of velocity fields from large Sc turbulent flow data and a variety of test fields. Based on (a) the relatively good accuracy demonstrated here for the demanding unity Schmidt number case in a full turbulent flow, (b) the fundamental improvement expected with increasing Sc, and (c) the results in Ref. 1, we expect that for $Sc \gg 1$ data the method should accurately determine velocity and velocity gradient fields in turbulent flows.

4. Experimental turbulent flow field results

In this section, we apply the scalar imaging velocimetry technique to fully resolved, four-dimensional, experimental data for $Sc \gg 1$ scalar mixing in a turbulent shear flow, and from this extract the first experimental measurements of the underlying structure and dynamics of the full velocity gradient tensor field in a turbulent flow. The data used here are for the mixing of a dynamically

passive Sc ≈ 2075 conserved scalar in the self-similar far field of an axisymmetric turbulent jet at outer-scale Reynolds number $Re_\delta = 4{,}200$.

An example of a typical two-dimensional spatial data plane from such a four-dimensional spatio-temporal data space is shown in Fig. 6*a*. Each such data plane has nominal dimensions of 256 × 256 data points, and spans 2.2 strain-limited viscous diffusion length scales ln on each side, or approximately 1/25-th of the local jet width. Note that $\lambda_v \approx 5.9 \cdot \lambda_K$, where $\lambda_K \equiv (\nu^3/\varepsilon)^{1/4}$ is the classical Kolmogorov scale. With the finest scalar gradient length scale being $\lambda_D = \lambda_v \cdot Sc^{-1/2}$, these scalar field data are fully resolved in all three spatial dimensions. In particular, the in-plane pixel spacing is $\Delta x = \Delta y \approx 107$ mm, and the effective interplane spacing is $\Delta z = 110$ mm, while the local scalar diffusion length scale λ_D is 239 mm. Further, the time separation between measurements at the same spatial point in two temporally successive three-dimensional spatial data volumes is $\Delta t = 0.0532$ sec. This compares with the local scalar gradient advection timescale λ_D/U of 0.0848 sec, indicating that the data are essentially resolved in time as well. This level of resolution, together with the high signal quality attained, allows accurate differentiation of the measured scalar field data simultaneously in all three space dimensions and in time. Examples of typical resulting $\partial\zeta/\partial t$, $\nabla\zeta$, and $\nabla^2\zeta$ fields are shown in Figs. 6*b-d*. All derivatives are obtained here by direct linear central differencing on the measured scalar field data. Notice that even the second derivatives in Fig. 6*d* are relatively free of the effects of noise. The variational nature of the implementation outlined in Section II for scalar imaging velocimetry should make the results obtained relatively insensitive to the errors that even this low level of noise introduces in (1).

Since Sc ≈ 2075 in these measurements, the ratio of the finest gradient length scales in the velocity and scalar fields is $\lambda_v/\lambda_D \approx 45$, and as a consequence measurements such as these that fully resolve the scalar field are highly oversampled for the velocity field. For this reason we subsample each of the scalar derivative planes in the four-dimensional data space to 128 × 128 points. This reduces considerably the computational work required to find the velocity field. The resulting **u** and **b** vectors each contain 61,440 elements; the same linear iteration algorithm used in Section III then typically requires less than one hour to solve the linear system for the velocity field $\mathbf{u}(\mathbf{x},t)$ in (12) at each time t.

A. *Vector velocity fields*

Fig. 7 shows the resulting u, v, and w components of the velocity vector field in the same scalar field data plane shown in Fig. 6. For the coordinate orientation used, u gives the radial component, v the streamwise component, and w the azimuthal (out of plane) component. The mean velocity has been subtracted from these components, so that the instantaneous fluctuation values are shown. The apparent length scale characteristics of the velocity gradients in these results is quite consistent with the above estimate that each data plane spans approximately 2.2 velocity gradient length scales in each direction. It should be noted that full three-component velocity vector field measurements such as these have not previously been available, and thus it is not common to present velocity field information in the form shown in Fig. 7. More typically, experimental velocity component fields are

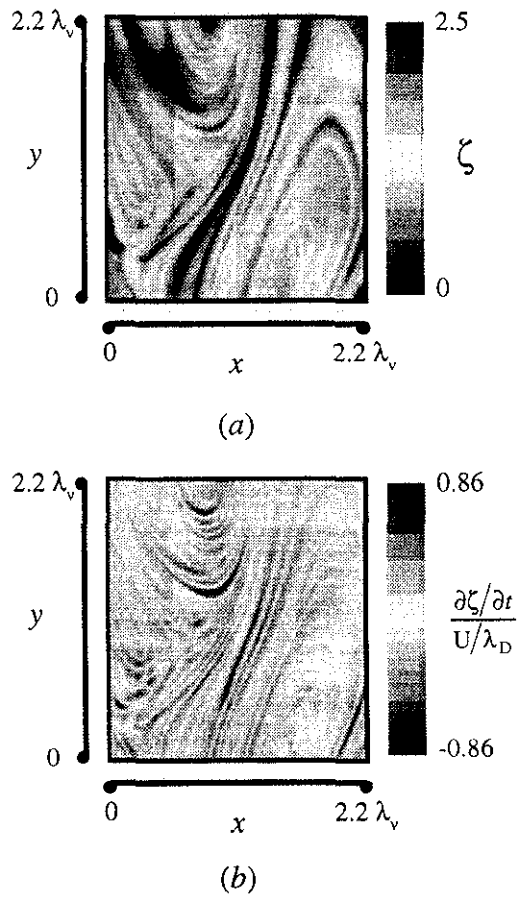

Figure 6 (continued next page).

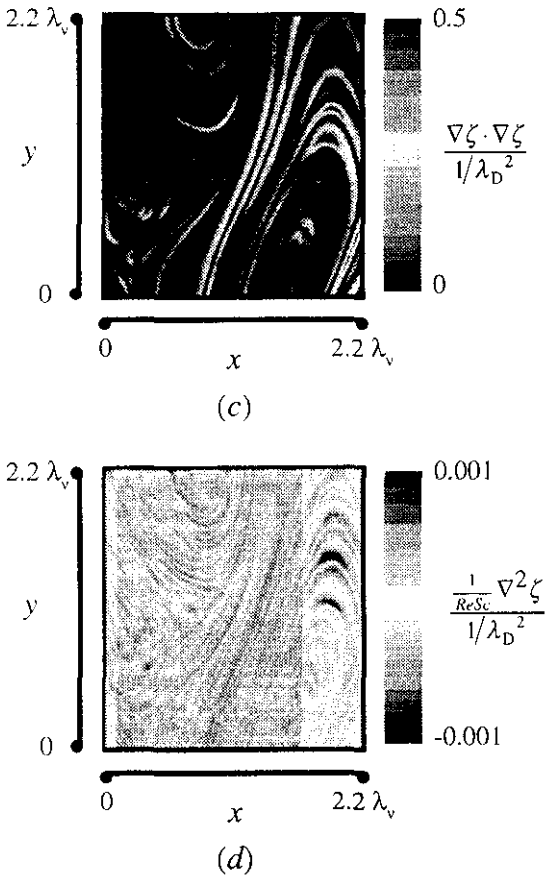

Figure 6. A turbulent flow scalar field and its derivatives. (*a*) the scalar field. (*b*) $\partial\zeta/\partial t$, (*c*) $\nabla\zeta\cdot\nabla\zeta$, (d) $\nabla^2\zeta$.

presented as projections of the local vectors into a measurement plane. For this reason, the data from Fig. 7 are shown in this manner in Fig. 8, where the (*u*,*v*) and (*u*,*w*) projections at each point in that particular plane are given.

It is apparent from the data in Figs. 7 and 8 that, owing to the large *Sc* involved, these measurements allow examination of the velocity field at the dissipative scales of turbulent flows. Results for the full vector velocity field over a larger range of length scales requires similarly resolved scalar field measurements at a significantly lower value of *Sc*, since $\lambda_v/\lambda_D = Sc^{1/2}$. The class of scalars for which practical measurements of the type required here are feasible is quite limited. The most promising among these appears to be the temperature field, which can be measured via the temperature-dependent collisional de-excitation rate of certain laser dyes. In that case $Sc \approx 7$, and thus the range of length scales in the velocity field accessible to the measurements is over 17 times larger than in Figs. 7 and 8. This would allow spatial measurements over length scales extending from the dissipative range into the inertial range. For the moment, we concentrate on the velocity gradient fields associated with vector velocity field measurements of the type in Figs. 7 and 8.

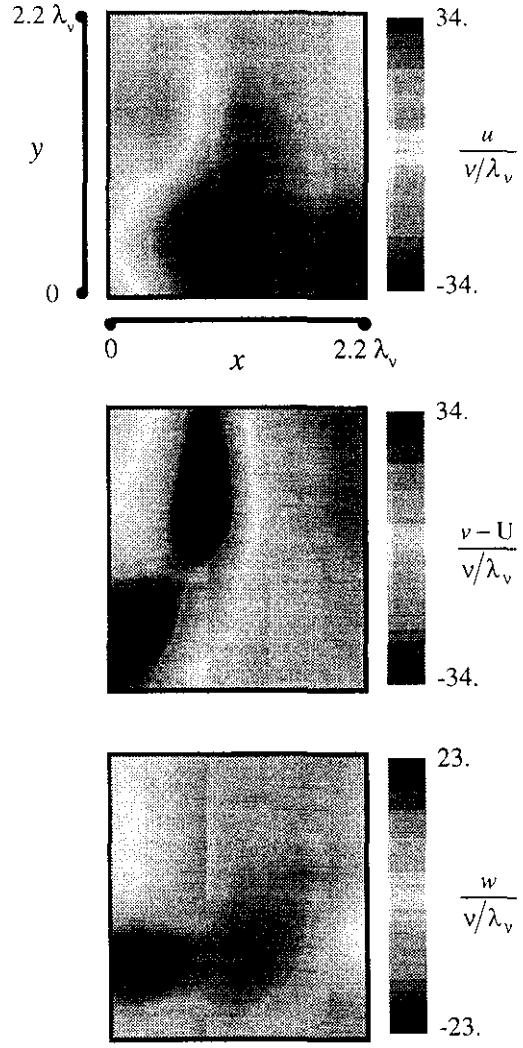

Figure 7. SIV results for the experimental scalar field measurements of Fig. 6. (top) the *u*-component of the velocity field. (center) the *v*-component, with the mean streamwise component subtracted. (bottom) the *w*-component.

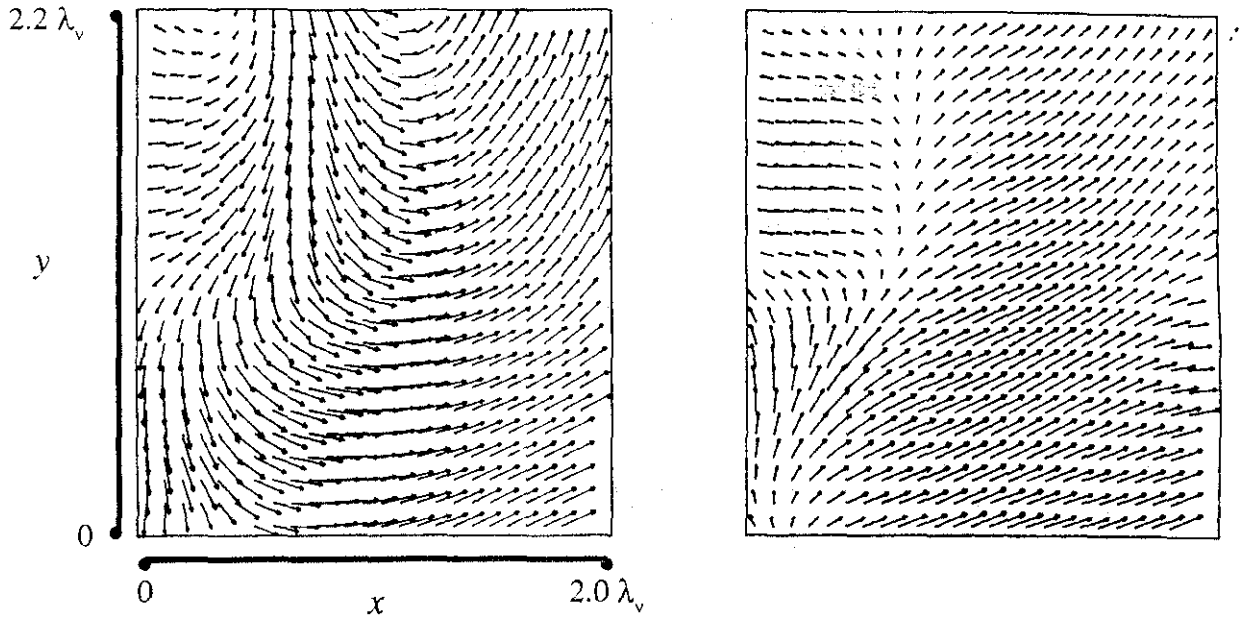

Figure 8. Projections of the SIV velocity vector results of Fig. 7 onto the x-y plane. (left) the u- and v- components, (right) the u- and v-components.

B. Velocity gradient tensor fields

Velocity vector field measurements in any given three-dimensional spatial data volume, formed from parallel planes of the type in Figs. 7 and 8, allow simultaneous differentiation of each of the u, v, and w components in x, y, and z to determine the full nine-component velocity gradient tensor. Of particular interest for dynamical studies of the small scales of turbulence are the symmetric and antisymmetric parts of this tensor. Fig. 9 shows the normal strain rate tensor field components $\varepsilon_{ii}(\mathbf{x},t)$ in the same plane for which results were given in Figs. 7-8. The vorticity vector field components $\omega_i(\mathbf{x},t)$ in the same plane, formed from the antisymmetric velocity gradient tensor components, are also shown in Fig. 9. From such individual velocity and velocity gradient component fields, we can examine dynamical quantities of interest such as the kinetic energy density field $k(\mathbf{x},t) \equiv 1/2\ \mathbf{u}\cdot\mathbf{u}(\mathbf{x},t)$, and the kinetic energy dissipation rate field $\Phi(\mathbf{x},t) \equiv 2\nu\ \varepsilon_{ij}\ \varepsilon_{ij}(\mathbf{x},t)$. Moreover, interactions between the symmetric and antisymmetric tensor components, such as the enstrophy production rate $W(\mathbf{x},t) \equiv \omega_i\ \varepsilon_{ij}\ \omega_j(\mathbf{x},t)$ and the scalar dissipation production rate $Z(\mathbf{x},t) \equiv \nabla\zeta_i\ \varepsilon_{ij}\ \nabla\zeta_j(\mathbf{x},t)$, are of particular dynamical interest and can be examined with very high resolution from measurements such as those in Figs. 6-9.

Studies of all these fields require knowledge of the full nine-component velocity gradient tensor field, which can be found easily from the SIV velocity field results; sample components of the tensor field are given in Fig. 9. Such laboratory measurements of the velocity gradient field on the small scales of a turbulent flow have not previously been possible. There are four key aspects of the present measurements that collectively make them unique. Firstly, the scalar imaging velocimetry measurements demonstrated here, giving the velocity gradient tensor at the small scales of turbulent flows, are fully resolved. Previous measurements with similar aims have been limited to significantly coarser resolution levels, which at least partially corrupt the gradient tensor components, since these are highly sensitive to resolution. [It should be noted that the experimentally measured velocity gradient fields in Fig. 9 are highly resolved even in comparison with those typically obtained from direct numerical simulation (DNS) studies of the small scales of turbulence. This is evident by comparing the fields in

Figs. 7-9 with typical DNS fields.] Secondly, the present measurements are entirely noninvasive, in contrast to earlier measurements based on multiple hot wire probes. As a consequence, the measurements themselves do not alter the quantities being measured. Thirdly, unlike most previous measurements of the gradient tensor components, the present scalar imaging velocimetry technique inherently produces all nine components of this tensor. Most previous probe-based measurements as well as optically based techniques have been limited to some subset of these. Finally, in contrast to probe-based methods, which are inherently single-point techniques producing time series data for the gradient components at a single point, the present measurements produce these at a very large number of points sufficiently closely spaced in both space and time to define the continuum fields. These are thus field measurements, as opposed to point measurements, and allow experimental examination not only of statistics of the velocity gradient components, but of the underlying spatiotemporal structure and dynamics in these dynamical fields at the small scales of turbulence.

C. Temporal evolution of the velocity gradient field

Results presented in the previous sections have been for the spatial structure of the velocity gradient tensor field at a fixed instant in time. However, the four-dimensional nature of the scalar field data on which these velocity field measurements are based allows the system defined by (9) - (11) to be solved at each time step Δt. Accordingly, the time evolution of any of the fields in the previous section can be examined by repeating the solution of (9) - (11) at the requisite times and assembling the fields of interest in time as shown, for instance, in Fig. 10. This figure presents the time-varying kinetic energy density field $k(\mathbf{x},t)$ and the corresponding kinetic energy dissipation rate field $\Phi(\mathbf{x},t)$ in the same spatial plane for which results were shown in Figs. 7-9, at 10 sequential instants in time. The time axis is measured in the inner variable $(t \cdot \nu/\lambda_\nu^2)$, where $t = 0$ corresponds to the instant for which the results were shown in Figs. 7-9.

Note that, just as the fully resolved $Sc \gg 1$ scalar field data oversamples the velocity field in space, the requisite time resolution demanded of the scalar field measurements leads to a Δt between successive three-dimensional spatial data volumes that is smaller than needed to resolve fully the time evolution of $\mathbf{u}(\mathbf{x},t)$. The results in Fig. 10 are thus shown at time intervals spaced 3 Δt apart. Clearly the structure in these planes is well correlated from one

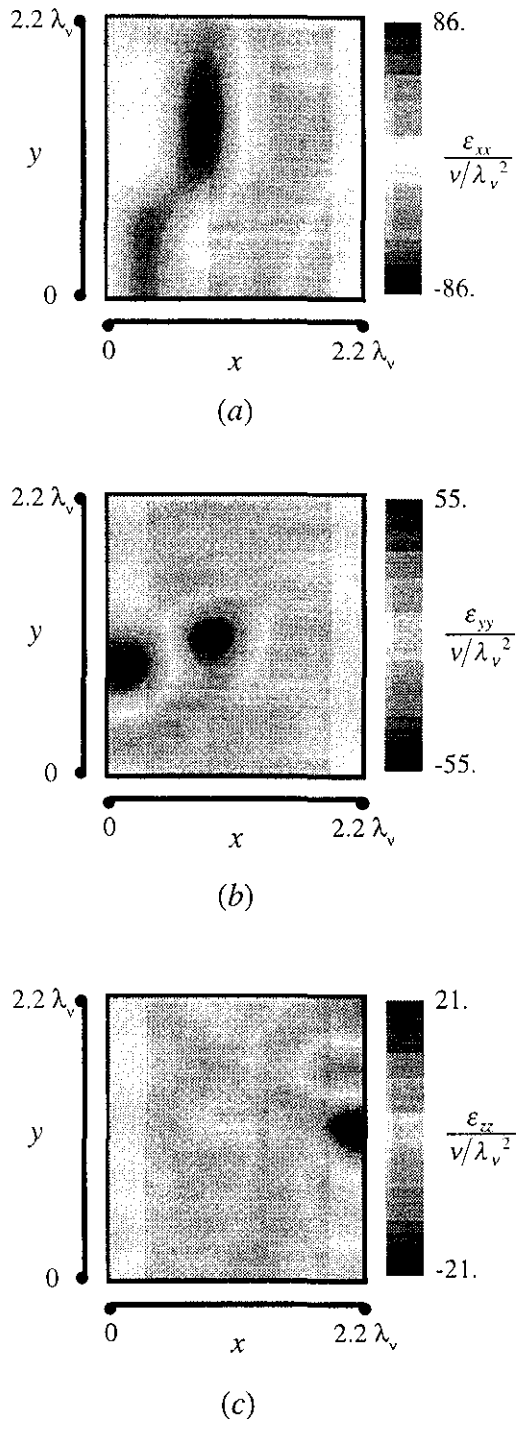

Figure 9. The normal strain components for the SIV results of Figs. 7, 8. (*a*) ε_{xx}, (*b*) ε_{yy}, (*c*) ε_{zz}. (Continued next page.)

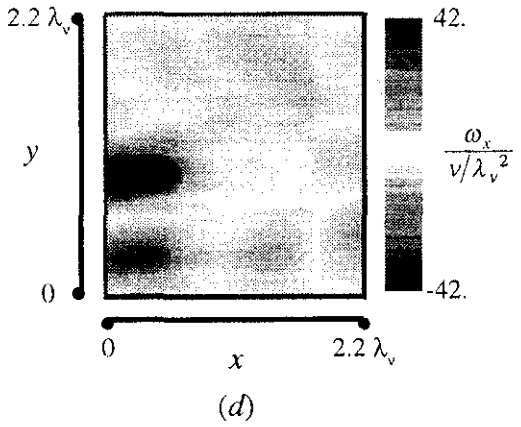

(*d*)

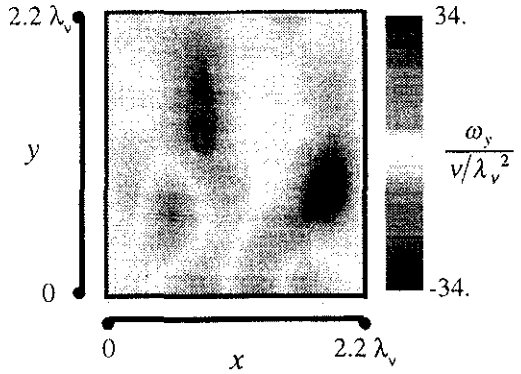

(*e*)

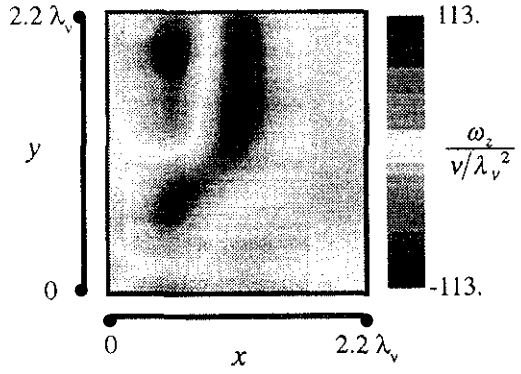

(*f*)

Figure 9 (*cont.*). The components of the vorticity vector ω, from the SIV results of Figs. 7, 8. (*d*) ω_x, (*e*) ω_y, (*f*) ω_z.

time step to the next, and further, the planes describe a clear temporal evolution of the flow. This is significant because, for this spacing in time, there is no common scalar field data involved in any of these time steps. No two planes share scalar field information in the scalar imaging velocimetry implementation in (3)-(11). Thus noise in the scalar field data is uncorrelated from one time step to the next. As a consequence, if the formulation implemented here to find the velocity field were sensitive to noise, there would be no a priori reason why the same field at two successive times in Fig. 10 should demonstrate a strong correlation or a clear evolution. The strong correlation of the results therefore must be ascribed to the fundamental well-posedness of the variational formulation. Moreover, while the results shown are spaced 3 Δt apart, the availability of the velocity gradient field components at all intermediate times permits accurate differentiation of the results to yield the detailed time evolution of the fine scales of turbulent flows.

5. Concluding remarks

This scalar imaging velocimetry technique offers experimental access to the spatial structure and time evolution of the full nine-component velocity gradient tensor in turbulent flows. These experimental results allow a level of detailed investigation of the dynamics of the small scales of turbulent flows that has previously been conceivable only through DNS studies. For high Schmidt number, the SIV results actually provide higher resolution of the fine scales than is currently possible by such direct numerical simulations. The availability of experimental techniques for measuring the requisite scalar field information has been well documented. The scalar imaging velocimetry technique thus is currently well suited to investigations of the fine structure and dynamics of the inner scales of turbulent flows.

Comparisons of the DNS and experimental scalar fields (Figs. 2 and 6, respectively) and the corresponding velocity fields (Figs. 3, 7) demonstrate clearly the differing character of the low and high Schmidt number limits. While the experimental scalar field appears to have finer characteristic length scales than the DNS scalar field, the DNS velocity field clearly has much finer length scales than does the experimental field. In particular, comparison of the fields emphasizes the variance in characteristic velocity and scalar length scales, which goes as $Sc^{1/2}$, and also shows the degree to which the $Sc = 1$ limit is a demanding one for the SIV technique.

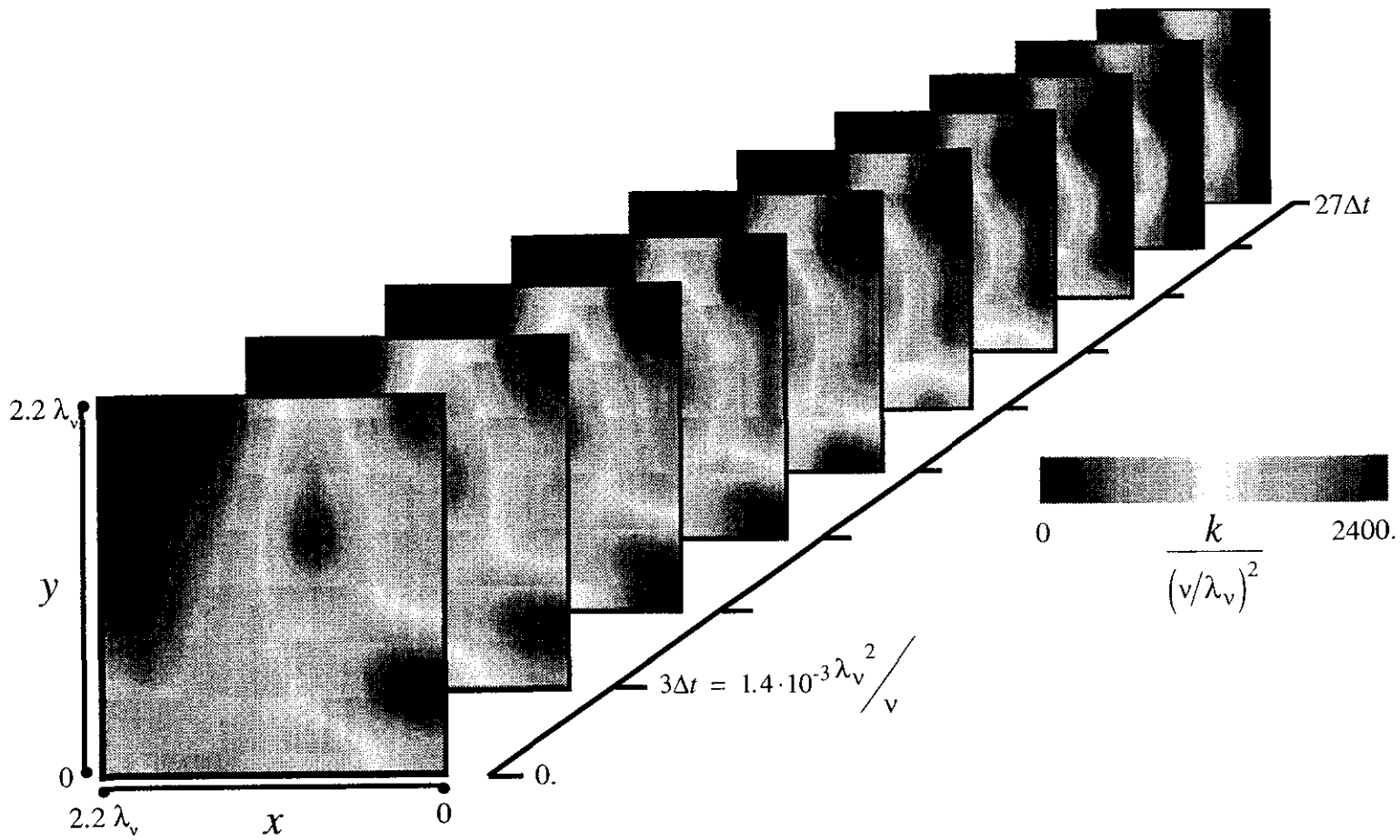

Figure 10*a*. The time evolution of the kinetic energy density field $k(\mathbf{x},t)$.

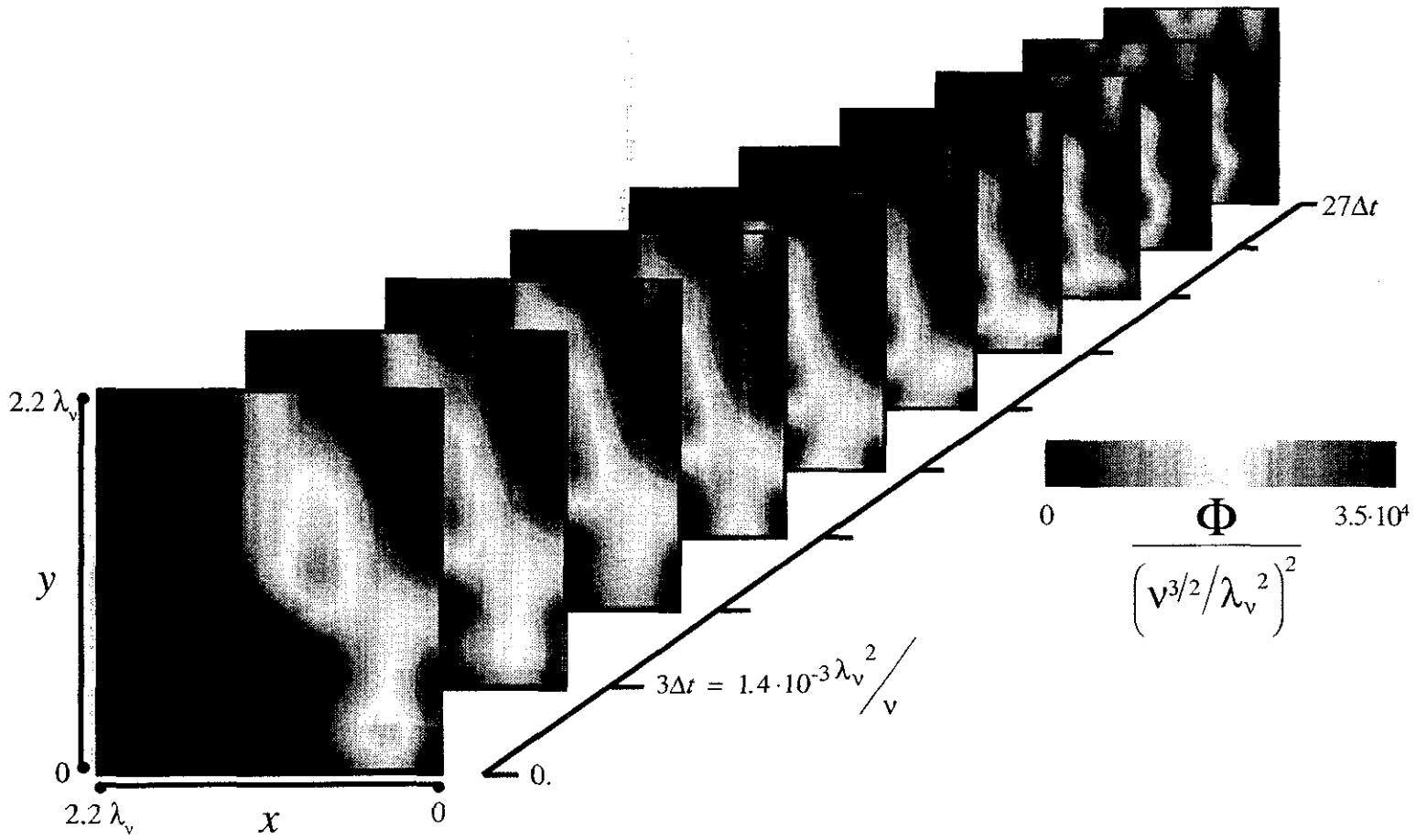

Figure 10*b*. The time evolution of the kinetic energy dissipation rate $\Phi(\mathbf{x},t)$.

At present, scalar field data which is sufficiently resolved to permit application of the scalar imaging velocimetry technique is only available for flows with $Sc \gg 1$. Thus the realm of $Sc \approx 1$ flows, e.g. the gas phase flows of particular interest in combustion applications, remains inaccessible to this velocimetry method. However, the lack of suitable scalar field diagnostics is the only limitation; as shown in §4, fully resolved $Sc = 1$ scalar field information is fully amenable to the scalar imaging velocimetry technique.

Currently, we are working to obtain spatially and temporally resolved measurements of the temperature field in turbulent flows. Preliminary results suggest that these temperature field measurements are feasible using the same approach used here to obtain measurements of the dissipative scales of motion in turbulent flows, though special issues attendant to the use of dyes with temperature-dependent fluorescence properties need to be addressed before fully resolved temperature field measurements in turbulent flows become practical. Temperature has a Schmidt number in water of approximately 7, so in the context of scalar imaging velocimetry the attractiveness of using temperature information is clear. Temperature field measurements would yield a view of the flow field that is $(2075/7)^{1/2} \approx 17$ times larger than that for the results presented here for $Sc \approx 2075$, given an equivalent level of scalar field resolution. That would permit experimental measurements of the full velocity gradient tensor over length scales extending from the dissipative scales into the inertial range, thereby allowing laboratory studies of subgrid scale dynamics.

Acknowledgements

This work is supported by the Air Force Office of Scientific Research (AFOSR) under AFOSR Grant No. F49620-92-J-0025. We are grateful to W.E. Mell, G. Kosály, and J.J. Riley at the University of Washington for providing the DNS data used in the $Sc = 1$ turbulent scalar field test cases. The experimental $Sc \gg 1$ scalar field measurements used for the present turbulent velocity field results were made by Kenneth B. Southerland at Michigan. An expanded version of this paper is being prepared for submittal to *Physics of Fluids*.

References

[1] Dahm, W.J.A., Su, L.K. & Southerland, K.B. (1992) A scalar imaging velocimetry technique for fully resolved four-dimensional vector velocity field measurements in turbulent flows. *Phys. Fluids A* **4**, 2191.

[2] Lang, D.B. (1985) Laser Doppler velocity and vorticity measurements in turbulent shear layers. Ph.D. Dissertation, Caltech, Pasadena.

[3] Adrian, R.J. (1986) Multi-point optical measurements of simultaneous vectors in unsteady flow - a review. *Int. J. Heat & Fluid Flow* **7**, 127-145.

[4] Adrian, R.J. (1991) Particle-imaging techniques for experimental fluid mechanics. Ann. Rev. Fluid Mech. **23**, 261-304.

[5] Lauterborn, W. & Vogel, A. (1984) Modern optical techniques in fluid mechanics. Ann. Rev. Fluid Mech. **12**, 223-244.

[6] Gad-el-Hak, M. (1989) Advances in Fluid Mechanics Measurements, Springer, Berlin.

[7] Nishino, N. Kasagi & Hirata, M. (1989) Three-dimensional particle tracking velocimetry based on automated digital image processing; *J. Fluids Eng.* **111**, 384.

[8] Papantoniou, D. & Maas, H.-G. (1990) Recent advances in 3-D particle tracking velocimetry; in Proceedings of the 5th Symposium on Applications of Laser Techniques to Fluid Mechanics (Instituto Superior Tecnico, Lisbon).

[9] Haussmann, G. & Lauterborn, W. (1980) Determination of size and position of fast moving gas bubbles in liquids by digital 3-D image processing of hologram reconstructions; *Appl. Opt.* **19**, 3529.

[10] Malyak, P.H. & Thompson, B.J. (1984) Particle displacement and velocity measurement using holography; *Opt. Eng.* **23**, 567.

[11] Scherer, J. & Bernal, L.P. (1988) Resolution characteristics of holographic particle image velocimetry; AIAA Paper No. 92-0009, AIAA, Washington, D.C.

[12] Dahm, W.J.A. & Buch, K.A. (1990) High-resolution three-dimensional spatiotemporal measurements of the conserved scalar field in turbulent shear flows; in Turbulent Shear Flows (Springer-Verlag, Berlin).

[13] Dahm, W.J.A., Southerland, K.B. & Buch, K.A.

(1991) Four-dimensional laser induced fluorescence measurements of conserved scalar mixing in turbulent flows; in Applications of Laser Techniques to Fluid Mechanics (Springer-Verlag, Berlin).

[14] Dahm, W.J.A., Southerland, K.B. & Buch, K.A. (1991) Direct, high-resolution, four-dimensional measurements of the fine scale structure of $Sc \gg 1$ molecular mixing in turbulent flows, *Phys. Fluids A* **3**, 1115.

[15] Dahm, W.J.A. (1992) Experimental studies of the fine scale structure of mixing in turbulent flows. Invited Paper, Proceedings of the Thirteenth Symposium on Turbulence, University of Missouri-Rolla, Rolla, MO.

[16] Truesdell, C., The Kinematics of Vorticity, Indiana Univ. Press, 1954.

[17] Dahm, W.J.A., Su. L.K & Southerland, K.B. (1992) Scalar imaging velocimetry measurements of vector velocity, vorticity and tensor strain rate fields in turbulent flows. Proceedings of the 6th International Symposium on Applications of Lasers in Fluid Mechanics, pp. 3.1.1-3.3.6, Instituto Superio Técnico, Lisbon, Portugal.

[18] Southerland, K.B. and Dahm, W.J.A. (1994) Four Dimensional Laser Induced Fluorescence Study of the Structure of Molecular Mixing in Turbulent Flows; AIAA Paper No. 94-0820, AIAA, Washington, D.C..

[19] Mell, W.E., G. Kosály, and J.J. Riley (1992) Private communication.